

Revision 3 for American Mineralogist

July 2016

## **Effect of iron and trivalent cations on OH-defects in olivine**

Marc Blanchard<sup>1</sup>, Jannick Ingrin<sup>2</sup>, Etienne Balan<sup>1</sup>, István Kovács<sup>3</sup>, Anthony  
C. Withers<sup>4</sup>

<sup>1</sup> Institut de Minéralogie, de Physique des Matériaux, et de Cosmochimie (IMPMC), Sorbonne Universités, UPMC Univ Paris 06, UMR CNRS 7590, Muséum National d'Histoire Naturelle, UMR IRD 206, 4 place Jussieu, F-75005 Paris, France

<sup>2</sup> UMET, UMR CNRS 8207, Université de Lille1, Bât. C6, 59655 Villeneuve d'Ascq, France

<sup>3</sup> Geological and Geophysical Institute of Hungary, Budapest, Stefánia street 14, H-1143, Hungary

<sup>4</sup> Department of Earth Sciences and Centre for Planetary Science and Exploration, University of Western Ontario, London, ON, Canada N6A 5B7

\*Communicating Author: Marc Blanchard. E-mail: [marc.blanchard@impmc.upmc.fr](mailto:marc.blanchard@impmc.upmc.fr)

## Abstract

Hydrogen incorporation in olivine involves many OH-defects, which will control the hydrogen solubility at mantle conditions. Several of these OH-defects are identified from the investigation of forsterite (the olivine Mg end-member). We study here the effect of  $\text{Fe}^{2+}$ ,  $\text{Fe}^{3+}$ ,  $\text{Al}^{3+}$  and  $\text{Cr}^{3+}$  on OH-defects in order to improve our understanding of the hydrogen speciation in natural olivine. Low-temperature infrared spectra ( $-194^\circ\text{C}$ ) are collected on synthetic and natural olivines. These spectra are then interpreted in the light of the theoretical determination of the structural, vibrational and infrared spectroscopic properties of Fe-related OH-defects, using first-principles calculations based on density functional theory. The presence of  $\text{Fe}^{2+}$  changes the cationic environment around the fully protonated vacancies in forsterite, leading to a slight modification of their infrared signatures. In particular, the presence of  $\text{Fe}^{2+}$  in an octahedral site adjacent to a hydrogarnet-type defect is likely responsible for the additional bands observed at  $3599\text{ cm}^{-1}$  and around  $3520\text{--}3550\text{ cm}^{-1}$  in Fe-doped olivines. Results show that the OH bands between  $3310$  and  $3380\text{ cm}^{-1}$  are associated with the presence of trivalent cations. Specifically, two bands at  $3323$  and  $3358\text{ cm}^{-1}$ , commonly observed in natural olivine, are associated with the substitution of  $\text{Mg}^{2+}$  by  $\text{Cr}^{3+}$  while two similar bands at  $3328$  and  $3353\text{ cm}^{-1}$  are associated with the substitution of  $\text{Mg}^{2+}$  by  $\text{Fe}^{3+}$ . The presence of these defects and the "titanoclinohumite" defect in natural olivine clearly underlines the prominent role of trace elements on the hydrogen incorporation in lithospheric olivine.

**Keywords:** olivine, OH-defect, iron, chromium, aluminum, IR spectroscopy, *ab initio* calculations, DFT

## 1. INTRODUCTION

The estimate of the amount of hydrogen stored in the olivine of the lithospheric and asthenospheric mantle (i.e., down to 410 km deep) is a key issue for understanding the internal cycle of this element. Attempts to constrain the hydrogen concentration in olivine from experimental solubility measurements may have been so far insufficient to accurately address this question (e.g., Bai and Kohlstedt 1992; Kohlstedt et al. 1996; Lemaire et al. 2004; Zhao et al. 2004; Smyth et al. 2006; Grant et al. 2007a; Litasov et al. 2007; 2009; Withers and Hirschmann 2008; Bali et al. 2008; Otsuka et Karato 2011; Withers et al. 2011; Férot and Bolfan-Casanova 2012; Kovács et al. 2012; Gaetani et al. 2014; Demouchy and Bolfan-Casanova 2016). The main reason for this possible inaccuracy lies in the fact that the incorporation of hydrogen into olivine is controlled by many mechanisms that are not clearly identified in most experimental studies. The evaluation and efficiency of different experimental approaches are strongly dependent on the correct identification of OH-defects. Without this knowledge, the risk of mixing the respective contributions of various defects and incorporation reactions that control their solubility is high. This identification is essential to ensure that the incorporation mechanisms reproduced in the laboratory are the same as those observed in natural samples, and thus to determine the dominant incorporation mechanisms (e.g., Mosenfelder et al. 2006; Gaetani et al. 2014).

Early solubility models in olivine were based on the assumption that the solubility is controlled by a single defect composed of two protons in an octahedral Mg vacancy (e.g., Kohlstedt et al. 1996; Zhao et al. 2004; Mosenfelder et al. 2006; Bali et al. 2008).

Increasing pieces of evidence indicate that this defect is, in fact, a minority point-defect. As evidenced by experiments performed under varying silica activities the protonation of Mg vacancies leads to broad infrared absorption bands in the range 3150-3250  $\text{cm}^{-1}$ , while the protonation of Si vacancies produces narrow infrared bands above 3480  $\text{cm}^{-1}$  (e.g., Lemaire et al. 2004; Berry et al., 2005; Kovács et al., 2010). Bond valence method (Donnay and Allmann 1970; Brown and Altermatt 1985) provides a simple explanation for this observation. In olivine, each O atom forms interatomic bonds with one  $\text{Si}^{4+}$  atom and three  $\text{Mg}^{2+}$  atoms, compensating for 1 and 1/3 valence units (v.u.), respectively. In octahedral  $\text{Mg}^{2+}$  and tetrahedral  $\text{Si}^{4+}$  vacancies, the deficit in valence compensation of the O atoms (i.e. residual valence) will be close to -1/3 or -1, respectively. Considering that the O-H bond valence regularly decreases as a function of O-H distance (Brown 2009), charge and valence compensation requirements lead to longer O-H bonds associated with Mg vacancies than with Si vacancies. Consistently, the OH stretching mode will vibrate at a higher frequency for protonated Si vacancies than for protonated Mg vacancies. Blanchard et al. (2013) applied successfully the bond valence analysis to wadsleyite, in order to identify the most favorable sites for protonation and to rationalize the OH infrared signatures. In the olivine case, this general picture has been confirmed and refined by atomistic modeling approaches (Haiber et al. 1997; Brodholt and Refson 2000; Braithwaite et al. 2003; Walker et al. 2006, 2007; Shaw and Tse 2007; Balan et al. 2011; 2014; Umemoto et al. 2011; Crépisson et al. 2014a; 2014b; Ingrin et al. 2014).

In the Mg end-member forsterite, infrared spectra in the range of OH stretching vibrations can be quite complex, but three types of OH-defects dominate. The hydrogarnet-type defect consisting of four protons in a tetrahedral Si vacancy, i.e.  $(4\text{H})_{\text{Si}}^{\times}$

using the Kröger-Vink notation (Kröger and Vink 1956), may represent about 70% of the incorporation mode at high-pressure, with absorption bands identified at 3612, 3577 and 3566  $\text{cm}^{-1}$  at room temperature (Berry et al. 2005; Kovács et al. 2010; Balan et al. 2011; Umemoto et al. 2011; Ingrin et al. 2013; Crépeisson et al. 2014a). The defect constituted of two protons in an octahedral Mg vacancy, i.e.  $(2\text{H})_{\text{Mg}}^{\times}$ , which is however very minor (<5%), results in a broad band between 3150 and 3250  $\text{cm}^{-1}$  (Berry et al. 2005; Kovács et al. 2010; Balan et al. 2011; Umemoto et al. 2011; Ingrin et al. 2013; Crépeisson et al. 2014a). A defect characterized by a broad band at 3550  $\text{cm}^{-1}$  and whose contribution in synthetic forsterite samples would approach 25% (Ingrin et al. 2013) may correspond to an interstitial OH (Balan et al. 2014). In presence of iron (olivine ~ Fo90), two types of additional OH stretching bands can be observed. The first band located at 3599  $\text{cm}^{-1}$ , is polarized parallel to the X direction and is significantly broader than the bands of the  $(4\text{H})_{\text{Si}}^{\times}$  defect (Kohlstedt et al. 1996; Smyth et al. 2006; Litasov et al. 2007; Otsuka and Karato 2011; Withers et al. 2011; Férot and Bolfan-Casanova 2012). Its contribution in synthetic samples can be up to 25% of the total OH concentration (with ~ 50% for the  $(4\text{H})_{\text{Si}}^{\times}$  defect and 25% for the defect related to the band to 3550  $\text{cm}^{-1}$ ). The second type of bands, between 3310 and 3380  $\text{cm}^{-1}$ , is mostly observed when natural samples are used as starting material in experiments (Bai and Kohlstedt 1993; Zhao et al. 2004; Grant et al. 2007a; Kovács et al. 2012; Férot and Bolfan-Casanova 2012; Gaetani et al. 2014, Yang 2016). Berry et al. (2007), from synthesis of forsterite samples doped with trace amounts of trivalent elements, suggested that these bands were associated with defects involving hydrogen and a trivalent cation, such as  $\text{Fe}^{3+}$ ,  $\text{Cr}^{3+}$  and  $\text{Al}^{3+}$ . Regarding the band at 3599  $\text{cm}^{-1}$ , no assumption has yet actually been proposed. All the above defects occur in

natural mantle olivine, with one additional defect resulting in a doublet of bands at 3525 and 3572  $\text{cm}^{-1}$ . It corresponds to a partially protonated tetrahedral vacancy coupled to the substitution of  $\text{Mg}^{2+}$  by  $\text{Ti}^{4+}$ , i.e.  $[(\text{Ti})_{\text{Mg}}^{\bullet\bullet}(\text{2H})_{\text{Si}}^{\prime\prime}]^{\times}$  (Berry et al. 2007; Balan et al. 2011; Umemoto et al. 2011).

We investigate here the effect of iron and trivalent cations on OH-defects in olivine. We performed an *in situ* study of OH infrared stretching bands at  $-194^{\circ}\text{C}$  and  $+25^{\circ}\text{C}$  on two Fe-bearing olivine single crystals, one synthetic and one natural. These spectroscopic measurements are coupled with the theoretical investigation of the structural and vibrational properties of Fe-related OH-defects using the density functional theory. OH-defects in only the Mg end-member olivine have so far been investigated using first-principles calculations. The explicit modeling of the infrared signature of these OH-defects allows untangling the effect of  $\text{Fe}^{2+}$ ,  $\text{Fe}^{3+}$ ,  $\text{Al}^{3+}$  and  $\text{Cr}^{3+}$  on the population of OH-defects. This study, we believe, represents one step forward in the understanding of hydrogen incorporation mechanisms in mantle olivines.

## 2. SAMPLES AND METHODS

### 2.1. Samples description

Three samples have been investigated here. The single crystal of composition Fo91 ( $\text{Mg}_{1.82}\text{Fe}_{0.18}\text{SiO}_4$ ) is from run M449 of Withers et al. (2011). It was synthesized from a mixture of oxides and hydroxides at 6 GPa and  $1250^{\circ}\text{C}$ , and contains 1212 ppm  $\text{H}_2\text{O}$ . Two natural olivine crystals (Fo91,  $\text{Mg}_{1.82}\text{Fe}_{0.17}\text{Ni}_{0.01}\text{SiO}_4$ ) with a reported water content of 4.2 ppm  $\text{H}_2\text{O}$  were also used for the study. They were extracted from a doubly

polished thin section cut from a spinel lherzolite xenolith (KHL8306) from Kilbourne Hole, New Mexico (Grant et al. 2007b), and oriented in the XY and XZ planes using the signature of the polarized FTIR spectra in the Si-O overtones region (see for instance, Lemaire et al. 2004). The composition and petrologic characteristics of the xenolith are reported in Grant et al. (2007b).

## **2.2. Infrared analysis**

IR spectra were acquired with a Bruker Hyperion 3000 FTIR-microscope coupled to a Bruker Vertex 70 spectrometer equipped with a liquid-N<sub>2</sub>-cooled MCT detector in the laboratory of Infrared and Raman Spectrochemistry (LASIR, Université Lille 1). A spot size of 160 × 160 μm<sup>2</sup> was used, 256 scans were accumulated per spectrum with a resolution of 1 cm<sup>-1</sup> to 4 cm<sup>-1</sup>. Polarized spectra were recorded with a wire grid polarizer on a KRS-5 substrate. A Linkam FTIR600 heating-cooling stage with ZnSe windows dedicated to infrared measurements was used. Band frequency was analyzed through decomposition of spectra using Gaussian functions in the “Peakfit” software.

## **2.3. First-principles calculations**

Calculations were performed within the density functional theory framework, using the theoretical approach and parameters described in Balan et al. (2011; 2014), Crépisson et al. (2014a; 2014b), and Ingrin et al. (2014) for the study of OH-defects in forsterite. The ionic core of iron, aluminum and chromium were described by the pseudopotentials Fe.pbe-nd-rrkjus.UPF, Al.pbe-rrkj.UPF and Cr.pbe-sp-van.UPF from <http://www.quantum-espresso.org/>. Spin-polarized calculations were conducted using the

generalized gradient approximation (GGA) to the exchange-correlation functional with the PBE parameterization (Perdew et al. 1996). The electronic wave-functions and the charge density were expanded in plane-waves with 80 and 480 Ry cut-offs, respectively. The Brillouin zone was sampled at a single  $k$ -point with coordinates (-0.5, -0.46, -0.4) in  $2\pi/a$  units. In order to prevent spurious interactions between the periodic images of the defect, structure relaxations were done on a  $2\times 1\times 2$  supercell of forsterite (112 atoms) using the PWscf code of the Quantum Espresso package (Giannozzi et al., 2009; <http://www.quantum-espresso.org>). The theoretical relaxed primitive orthorhombic-cell parameters of anhydrous forsterite are  $a = 4.78 \text{ \AA}$ ,  $b = 10.28 \text{ \AA}$ , and  $c = 6.01 \text{ \AA}$  ( $Pbnm$  space group), in good agreement with experimental values (Fujino et al., 1981). These relaxed cell parameters were kept constant during the relaxation of OH-bearing supercell. During this step, no symmetry constraint was applied to the atomic positions and the forces on atoms were minimized to less than  $10^{-4}$  Ry/a.u. The OH-stretching vibrational frequencies were calculated at the Brillouin zone center ( $\Gamma$  point), using the linear response theory (Baroni et al., 2001) as implemented in the PHonon code (Giannozzi et al., 2009; <http://www.quantum-espresso.org>) and following the approach previously used by Balan et al. (2011; 2014), Crépisson et al. (2014a; 2014b), and Ingrin et al. (2014). This approach provides calculated wavenumbers that are within 1.5 % of the measured ones for the OH stretching vibrations (i.e.  $< 50 \text{ cm}^{-1}$ ). This approach is very sensitive to the strength of hydrogen bonds, giving very accurate relative positions of infrared absorption bands. The relative positions of the bands combined with their intensities and pleochroisms allow their reliable assignment to associated OH-defects by comparison of theoretical and measured infrared spectra.



### 3. RESULTS AND DISCUSSION

#### 3.1. Infrared spectrum of iron-bearing olivine

Low-temperature measurements allow a better resolution of every contribution to the infrared spectrum. As shown in Fig. 1 and Table 1, the infrared spectrum above 3500  $\text{cm}^{-1}$  of synthetic Mg end-member olivine is mainly composed of three bands at 3615, 3582 and 3568  $\text{cm}^{-1}$  corresponding to the hydrogarnet-type defect,  $(4\text{H})_{\text{Si}}^{\times}$  plus a side band at 3566  $\text{cm}^{-1}$ , which corresponds to the broad band strongly polarized along the Y direction observed at room temperature at 3550  $\text{cm}^{-1}$  (Balan et al. 2011; Ingrin et al. 2013). In the synthetic Fe-bearing olivine, additional bands are observed. A broad band reported at 3599  $\text{cm}^{-1}$  at room temperature and polarized along the X direction (Kohlstedt et al. 1996; Smyth et al. 2006; Litasov et al. 2007; Otsuka and Karato 2011; Withers et al. 2011; Férot and Bolfan-Casanova 2012), splits at  $-194^{\circ}\text{C}$  into two separate bands at 3606 and 3599  $\text{cm}^{-1}$  both mainly polarized along X (Fig. 1). At least three additional bands are also observed in the range 3520 – 3560  $\text{cm}^{-1}$ : At room temperature, along Y they are partly masked by the broad band at 3550  $\text{cm}^{-1}$ , but it is possible to notice the presence of at least two extra bands around 3549 and 3538  $\text{cm}^{-1}$  in the spectrum polarized perpendicularly to the Y direction (Fig. 1). At  $-194^{\circ}\text{C}$ , four distinct bands are clearly visible. The strongest at 3560 and 3551  $\text{cm}^{-1}$  are mainly polarized along Y while the ones at 3543 and 3528  $\text{cm}^{-1}$  share polarization between Y and the direction perpendicular to Y (Fig. 1). The additional bands, summed over the two polarized spectra, constitute roughly 40% of the total area of the OH bands.

The three main bands observed in the Mg end-member forsterite (3615, 3582 and 3568  $\text{cm}^{-1}$ ) are also present at the same wavenumbers but are broader in the Fe-bearing olivine Fo91. Nevertheless it is still possible to isolate the contribution of the band at 3568  $\text{cm}^{-1}$  polarized along the Z direction from the band at 3567  $\text{cm}^{-1}$  polarized along the Y direction in the spectra at  $-194^\circ\text{C}$  (see vertical line in Fig. 1; the band at 3567  $\text{cm}^{-1}$  corresponds to the band observed at 3566  $\text{cm}^{-1}$  in forsterite and which results from the shift of the broad band observed at 3550  $\text{cm}^{-1}$  at room temperature).

In the same frequency region, the natural olivine KHL8306 from Kilbourne Hole displays a different infrared signature (Fig. 2) characterized at low temperature by two bands at 3529 and 3576  $\text{cm}^{-1}$ , mainly polarized along the X direction and assigned to the “titanoclinohumite” defect,  $[(\text{Ti})_{\text{M1}}^{\bullet\bullet}(\text{2H})_{\text{Si}}^{\prime}]^{\times}$  (Berry et al. 2005; 2007; Balan et al. 2011). At lower frequency, the same sample displays a doublet of bands at 3332  $\text{cm}^{-1}$  mainly polarized along the Z direction and 3356  $\text{cm}^{-1}$  with its main contribution along the X direction. Two weak bands at 3313 and 3390  $\text{cm}^{-1}$ , mainly polarized along the Z direction, accompany this doublet. Such features are frequently observed when natural samples are used as starting material in experiments (Bai and Kohlstedt 1993, Zhao et al. 2004; Grant et al. 2007a; Férot and Bolfan-Casanova 2012; Gaetani et al. 2014). All OH absorption bands mentioned here exhibit a similar temperature evolution with a moderate frequency lowering when temperature increases ( $< 7 \text{ cm}^{-1}$  between  $-194^\circ\text{C}$  and  $25^\circ\text{C}$ ).

### 3.2. Effect of $\text{Fe}^{2+}$ on protonated Si and Mg vacancies

In a defect-free olivine, calculations indicate only a small preference (35 meV corresponding to 3.4 kJ/mol) for  $\text{Fe}^{2+}$  to occupy M1 sites against M2 sites. This energy

difference implies that at temperatures relevant to the upper mantle ( $\sim 1227^\circ\text{C}$ ), around 57% of  $\text{Fe}^{2+}$  will be in M1 sites. This result is in complete agreement with the nuclear magnetic resonance study of McCarty et al. (2015) concluding that  $\text{Fe}^{2+}$  occupies M1 and M2 roughly equally. Therefore no initial assumption was made regarding the location of  $\text{Fe}^{2+}$  around the OH-defects.

All possible configurations with one  $\text{Fe}^{2+}$  as a first neighbor around the  $(4\text{H})_{\text{Si}}^{\times}$  defect have been investigated. Protons were initially set up in the configuration Si<sub>3</sub> of Balan et al. (2011), which was found to be the most stable in forsterite as well as the one showing the best agreement with experimental spectra. The corresponding infrared signature is reported in Fig. 3. Calculations suggest that the most favorable location for  $\text{Fe}^{2+}$  is the M1 site sharing a corner with the Si vacancy, followed by the M2 site also sharing a corner with the vacancy with a total energy 43 meV (4.1 kJ/mol) higher (Table 2). This new cationic environment affects the OH-defect as highlighted by the variation of its infrared signature (Fig. 3). The corresponding structural and vibrational properties are reported in Table 2. Considering this energy difference and the fact that for  $[(4\text{H})_{\text{Si}}^{\times}(\text{Fe})_{\text{M1corner}}^{\times}]^{\times}$ , two equivalent configurations exist relative to the mirror plane crossing the silicate tetrahedron, we expect the occurrence of three times more  $[(4\text{H})_{\text{Si}}^{\times}(\text{Fe})_{\text{M1corner}}^{\times}]^{\times}$  defects than  $[(4\text{H})_{\text{Si}}^{\times}(\text{Fe})_{\text{M2corner}}^{\times}]^{\times}$  defects, at temperatures relevant to the upper mantle. The OH stretching mode at  $3591\text{ cm}^{-1}$  in forsterite is shifted to  $3573$  and  $3559\text{ cm}^{-1}$  when  $\text{Fe}^{2+}$  is in M1 and M2, respectively. This mode polarized along the X direction corresponds to the in-phase stretching of the four OH groups, with a larger displacement of the proton of the O1H group. The mode at  $3572\text{ cm}^{-1}$  in forsterite is shifted down to  $3556\text{ cm}^{-1}$  when  $\text{Fe}^{2+}$  is in M1 site but remains at the same frequency

when  $\text{Fe}^{2+}$  is in M2 site. In this mode, the O2H group vibrates out-of-phase relative to the three other OH groups and with the largest amplitude. A moderate change in geometry may affect the OH coupling pattern, significantly impacting the IR intensities. This may explain why only three absorption bands are observed experimentally in forsterite out of the four bands predicted theoretically (i.e., the band calculated at  $3572\text{ cm}^{-1}$  is not observed). It is reasonable to assign the band at  $3606\text{ cm}^{-1}$  observed in Fe-bearing olivine with a polarization along the X direction (Fig. 1, Table 1) to the most intense band calculated at  $3573\text{ cm}^{-1}$  and therefore to the presence of  $\text{Fe}^{2+}$  in a M1 site next to the hydrogarnet-type defect. The band at  $3599\text{ cm}^{-1}$  can be assigned to the most intense band of the defect associated with  $\text{Fe}^{2+}$  in the M2 site calculated at  $3559\text{ cm}^{-1}$ . The two lowest bands of these hydrogarnet-type defects are also shifted to lower frequencies in presence of iron. The mode at  $3520\text{ cm}^{-1}$  in forsterite remains polarized along the Z direction while the mode at  $3540\text{ cm}^{-1}$  shows some variations in the XY plane. Most of the bands observed at  $3560$ ,  $3551$ ,  $3543$  and  $3528\text{ cm}^{-1}$  can be assigned to the lower-frequency bands associated with  $\text{Fe}^{2+}$  in M1 and M2 sites calculated at  $3530$ ,  $3518\text{ cm}^{-1}$  and  $3519$ ,  $3510\text{ cm}^{-1}$ , respectively. They have the correct polarizations. However it cannot be ruled out that the intense band observed at low temperature at  $3560\text{ cm}^{-1}$  (parallel to the Y direction) could be equivalent to the band observed at  $3566\text{ cm}^{-1}$  in forsterite (Fig. 1), which become at room temperature the broad band at  $3550\text{ cm}^{-1}$  strongly polarized along the Y direction (absorption band assigned to an interstitial OH, Ingrin et al. 2013, Balan et al. 2014). The presence of a nearby  $\text{Fe}^{2+}$  would explain the simultaneous occurrence of these two bands and their frequency shift. In addition, the binding energies between  $\text{Fe}^{2+}$  and the hydrogarnet-type defect, which is defined as the energy of the reaction leading

the two defects to associate, were estimated to be -7 and -12 meV for  $\text{Fe}^{2+}$  in M1 and M2 sites, respectively. This suggests that there is almost no energy gain to combine the  $(\text{Fe})_{\text{M}}^{\times}$  and  $(4\text{H})_{\text{Si}}^{\times}$  neutral species. Their mutual arrangement will be statistical. According to the typical iron concentration in natural or synthetic sample ( $\sim\text{Fo}90$ ), the presence of more than one  $\text{Fe}^{2+}$  around the protonated Si vacancy should occur with a probability around 20%, and explain the complexity of the olivine infrared spectra in this high-frequency range.

Effect of  $\text{Fe}^{2+}$  on protonated Mg vacancies is expected in the range 3100-3300  $\text{cm}^{-1}$  of the infrared spectrum. Two bands polarized along the Z direction are often recorded at  $\sim 3160 \text{ cm}^{-1}$  and 3220-3260  $\text{cm}^{-1}$  in both Fe-free and Fe-bearing olivine samples. These two bands do not always occur simultaneously, their relative intensities vary, and a broadening seems to accompany the presence of iron (e.g., Lemaire et al. 2004; Withers et al. 2011; Schmädicke et al. 2013). Previous calculations have shown that the full protonation of a M1 vacancy is responsible for one of the two bands, presumably the one observed at 3160  $\text{cm}^{-1}$  in the Mg end-member (e.g., Balan et al. 2011). At the vicinity of this OH-defect,  $\text{Fe}^{2+}$  enters the M1 site sharing an edge with the vacancy or the M2 site sharing a corner with the vacancy (Fig. 4). The two configurations have nearly the same probability of occurrence (3 meV of energy difference). The presence of  $\text{Fe}^{2+}$  decouples the two OH vibrational modes (Fig. 4 and Table 2), leading to a band splitting of 40-54  $\text{cm}^{-1}$  depending on the models. OH groups remain aligned along the Z direction. While it is likely that the presence of iron may explain the broadening of the band related to the defect  $(2\text{H})_{\text{M1}}^{\times}$ , it cannot explain the two distinct bands that are also observed in Fe-free olivines. It is sometimes found in the literature that these two bands correspond to the

protonation of M1 and M2 vacancies (Lemaire et al. 2004). This has already been investigated by atomistic calculations (e.g., Walker et al. 2006; Shaw and Tse 2007; Umemoto et al. 2011) but the explicit modeling of the infrared signature was never made for the M2 vacancy. Of the eight starting configurations, the two most stable optimized geometries and the corresponding spectra are shown in Figs. S1 and S2. The configuration of lowest energy corresponds to the protonation of two O3 atoms belonging to an edge of the octahedral vacancy. The vibrations of these two O3H groups are coupled, leading to an intense band at  $3265\text{ cm}^{-1}$  polarized in the XY plane and a smaller band at  $3247\text{ cm}^{-1}$  polarized along the Z direction (Table 2). In the second configuration, the two O3H groups are located on either side of the vacancy center. With two significantly different OH bond lengths, their motions are decoupled leading to an intense band at  $3209\text{ cm}^{-1}$  polarized in the XY plane and a smaller band at  $3488\text{ cm}^{-1}$  polarized in the XZ plane. None of these defects presents the pleochroism of the two bands observed experimentally. Furthermore, in excellent agreement with the calculations of Umemoto et al. (2011), the defect  $(2\text{H})_{\text{M2}}^{\times}$  is 513 meV (49.5 kJ/mol) less stable than the defect  $(2\text{H})_{\text{M1}}^{\times}$ . From this energy difference and the comparison of calculated and measured pleochroisms, it is therefore possible to rule out the involvement of a simple protonated M2 vacancy for potential hydrogen substitutions. Finally as shown in Crépisson et al. (2014a), the partial protonation of a M1 vacancy is not a satisfactory explanation of the second absorption band around  $3220\text{ cm}^{-1}$ .

### 3.3. OH-defects involving trivalent cations

In a defect-free olivine, our calculations suggest that  $\text{Fe}^{3+}$  will preferentially occupy M2 rather than M1 sites. The energy difference of 173 meV (16.7 kJ/mol) would indicate a proportion of  $\sim 80\%$  of  $\text{Fe}^{3+}$  in M2 sites at  $\sim 1227^\circ\text{C}$ . However, the presence of Mg vacancies in the vicinity of  $\text{Fe}^{3+}$ , with the structural relaxation associated, will decrease significantly this energy difference. This is evidenced by the investigation of the defects composed of a proton in a Mg vacancy, the charge of which is compensated by the substitution  $\text{Mg}^{2+}-\text{Fe}^{3+}$  in a neighboring M site, i.e.  $[(\text{Fe})_{\text{M}}^{\bullet}(\text{H})'_{\text{M}}]^{\times}$ . This mechanism is the one proposed by Berry et al. (2007) for explaining the infrared absorption bands observed between 3300 and 3400  $\text{cm}^{-1}$ . The three most favorable configurations of this defect and the corresponding infrared signatures are shown in the upper part of Figs. 5 and 6. Even in close proximity of  $\text{Fe}^{3+}$ , the protonation of M1 vacancies is energetically preferred to the protonation of M2 vacancies (energy difference of  $\sim 860$  meV, i.e. 83 kJ/mol). In the most stable configuration,  $\text{Fe}^{3+}$  is in the M2 site sharing an edge with the M1 vacancy where the O3 atom is protonated, leading to a band at 3388  $\text{cm}^{-1}$  with the strongest contribution along the X direction. The second configuration has the  $\text{Fe}^{3+}$  in the M2 site sharing a corner with the vacancy. The O2 atom is protonated, which results in a band at 3245  $\text{cm}^{-1}$  polarized along the Z direction. In the third configuration,  $\text{Fe}^{3+}$  now occupies an M1 site. The proton is still bound to the O2 atom, leading again to a band mainly polarized along the Z direction but at a wavenumber of 3374  $\text{cm}^{-1}$ . The two highest bands could very well explain the bands that we observe at 3355 and 3329  $\text{cm}^{-1}$  (3356 and 3332  $\text{cm}^{-1}$  at low temperature) in Kilbourne Hole olivine (Fig. 2). Their relative positions and pleochroisms are in good agreement. The band calculated for the second configuration (i.e., 3245  $\text{cm}^{-1}$ ) is not observed in the Kilbourne Hole sample.

However, the small energy differences calculated between the three configurations (Table 2) would suggest their coexistence at mantle temperatures with proportions around 30-40 % each, which means that the doublet at 3355-3329  $\text{cm}^{-1}$  should be correlated with a band at 3220  $\text{cm}^{-1}$ . This is not the case in most of the natural samples of olivine.

Considering now the trivalent cation  $\text{Al}^{3+}$ , the most stable configuration  $[(\text{Al})_{\text{M2edge}}^{\bullet}(\text{1H})'_{\text{M1}}]^{\times}$  is the same as with  $\text{Fe}^{3+}$  (Fig. 6). The corresponding absorption band is only shifted by 2  $\text{cm}^{-1}$ . The second most stable configuration with  $\text{Al}^{3+}$   $[(\text{Al})_{\text{M1edge}}^{\bullet}(\text{1H})'_{\text{M1}}]^{\times} \text{A}$  is the same as the third configuration described for  $\text{Fe}^{3+}$ . The change of the cation nature shifts the band by  $\sim 10 \text{ cm}^{-1}$  while the polarization remains identical. The fact that the defects related to  $\text{Fe}^{3+}$  and  $\text{Al}^{3+}$  give rise to very similar absorption bands with the two bands of  $\text{Al}^{3+}$  much closer in frequencies than the bands associated to  $\text{Fe}^{3+}$  (1  $\text{cm}^{-1}$  for  $\text{Al}^{3+}$ ; 14  $\text{cm}^{-1}$  for  $\text{Fe}^{3+}$ ) is in full agreement with the observations of Berry et al. (2007; 6  $\text{cm}^{-1}$  for  $\text{Al}^{3+}$ ; 19  $\text{cm}^{-1}$  for  $\text{Fe}^{3+}$ ). Finally, the third most favorable defect with  $\text{Al}^{3+}$   $[(\text{Al})_{\text{M1edge}}^{\bullet}(\text{1H})'_{\text{M1}}]^{\times} \text{B}$  only differs from the second one by the protonation that occurs on the O3 atom instead of the O2 atom. The corresponding theoretical band is located at 3401  $\text{cm}^{-1}$  and is polarized along the X direction.

Tollan et al. (2015) studied the olivine of an arc mantle peridotite by coupling infrared spectroscopy and chemical analysis, and found that the incorporation of water in olivine is controlled by its  $\text{Cr}^{3+}$  and  $\text{Fe}^{3+}$  contents. We have then investigated defects similar to the previous ones but with  $\text{Cr}^{3+}$  instead of  $\text{Fe}^{3+}$ , i.e.  $[(\text{Cr})_{\text{M}}^{\bullet}(\text{1H})'_{\text{M}}]^{\times}$ . Two configurations were found close in energy, the others being significantly less stable ( $> 97 \text{ meV}$ ). In both,  $\text{Cr}^{3+}$  occupies the M1 site sharing an edge with the protonated M1 vacancy (Fig. 6). In the first configuration, the O2 is protonated giving rise to a band at



3366  $\text{cm}^{-1}$  polarized along the Z direction, while in the second configuration the protonation occurs in O3 and corresponds to a band at 3406  $\text{cm}^{-1}$  (Fig. 5).  $\text{Cr}^{3+}$ -bearing defects thus display infrared signatures comparable with the ones of  $\text{Fe}^{3+}$  and  $\text{Al}^{3+}$  in terms of pleochroism but with a larger gap in frequencies between the two bands (40  $\text{cm}^{-1}$ ). These results fully support the interpretation of Tollan et al. (2015) that the bands they observed at 3358 and 3323  $\text{cm}^{-1}$  are associated with  $\text{Cr}^{3+}$  while the bands around 3353 and 3328  $\text{cm}^{-1}$  are associated with  $\text{Fe}^{3+}$ .

Other OH-defects involving  $\text{Fe}^{3+}$  were explored. A  $\text{Si}^{4+}$  tetrahedral vacancy could be charge balanced by one  $\text{Fe}^{3+}$  and one  $\text{H}^+$ , i.e.  $(\text{Fe} + 1\text{H})_{\text{Si}}^{\times}$ . In the most stable geometry, the proton is bound to an O3 oxygen and points towards another O3 oxygen (Fig. S3). The corresponding infrared absorption band is calculated at 3140  $\text{cm}^{-1}$  with a polarization in the XY plane. No infrared band shows this polarization in synthetic or natural olivine samples. The presence of such a defect can thus be ruled out. This is in agreement with the fact that Mössbauer spectroscopy showed that  $\text{Fe}^{3+}$  occupies predominantly octahedral sites in olivine (McCammon et al. 2004). On the model of the “titanoclinohumite” defect, one could also propose a defect composed of a partially protonated Si vacancy compensated by one  $\text{Fe}^{3+}$  in a neighboring M site, i.e.  $[(\text{Fe})_{\text{M}}^{\bullet}(3\text{H})_{\text{Si}}^{\prime}]^{\times}$ . In the most stable configuration,  $\text{Fe}^{3+}$  occupies a M1 site sharing an edge with the tetrahedral vacancy (Fig. S4). This defect is characterized by three OH stretching bands. The two bands at 3474 and 3544  $\text{cm}^{-1}$  are very similar to the infrared signature of the “titanoclinohumite” defect (Balan et al. 2011). The additional band is at much lower wavenumber, 3255  $\text{cm}^{-1}$ , with the main contribution parallel to the X direction. Like for

the previous defect, such a band in this frequency region is never observed in olivine, ruling out the presence of this defect.

As shown in Fig. 2, the main doublet involving trivalent cations is accompanied by two weak bands at 3310 and 3384  $\text{cm}^{-1}$  (25°C). Although observed in some synthetic as well as natural samples, the band at 3384  $\text{cm}^{-1}$  is not systematically present when the three others are present. Berry et al. (2007) do not observe such a band in their doped forsterite crystals. Conversely, the presence of the band at 3310  $\text{cm}^{-1}$  polarized mainly along Z is systematic and the position of this band shifts with the nature of the trivalent cation, i.e. 3310  $\text{cm}^{-1}$  for  $\text{Fe}^{3+}$ , 3306  $\text{cm}^{-1}$  for  $\text{Cr}^{3+}$ , 3322  $\text{cm}^{-1}$  for  $\text{Al}^{3+}$  (Berry et al. 2007). The most stable OH-defects shown here cannot account for these bands and their origin remains an unsolved question.

### 3.4. Absorption coefficients

The quantification of the OH concentration using infrared spectroscopy relies on the knowledge of absorption coefficients. In order to get the most reliable results possible, one must use only the absorption coefficients derived from experimental calibrations because systematic discrepancies related to modeling approximations are expected. The computed absorption coefficients are, however, very useful in order to establish the expected trends of the absorption properties with the wavenumber of the OH stretching bands, with the nature of the OH-defects, or with the nature of minerals investigated. Figure 7 shows that the theoretical absorption coefficients of the OH-defects considered here define a trend consistent with the values of the OH-defects previously investigated in forsterite (Balan et al. 2011; 2014; Crépeisson et al. 2014a; 2014b; Ingrin et

al. 2014). This trend is almost parallel to the theoretical general correlation determined for OH groups in hydrous and anhydrous minerals (Balan et al. 2008), but downshifted. This suggests first that an olivine-specific calibration is recommended over general calibrations in order to get more accurate OH concentrations, which is consistent with previous studies (*e.g.*, Bell et al. 2003; Rossman 2006; Withers et al. 2012). Second, calculations indicate that for infrared bands around  $3600\text{ cm}^{-1}$ , the olivine-specific absorption coefficient should be  $\sim 50\%$  smaller than the value derived from a general correlation, while for bands around  $3200\text{ cm}^{-1}$  this downshift should be of  $\sim 25\%$ . These predictions are consistent with the observation that absorption coefficients in olivine tend to be smaller than those derived from general wavenumber-dependent calibrations (Bell et al. 2003; Aubaud et al. 2009; Kovács et al. 2010; Withers et al. 2012). Furthermore, these results underline that it is of primary importance to untangle the contribution of different substitution mechanisms in olivine in order to infer the actual hydrogen concentration.

#### 4. IMPLICATIONS

The assignment of OH bands motivated by theoretical considerations that allow prediction of the most probable configurations confirm, once again, that  $(2\text{H})_{\text{Mg}}^{\times}$  defects play a minor role compared to  $(4\text{H})_{\text{Si}}^{\times}$  and others in the water solubility of olivine at high pressure (Balan et al. 2011; Umemoto et al. 2011; Ingrin et al. 2013). A recent NMR study performed on a forsterite sample synthesized at 12 GPa reached the same conclusion (Xue et al. 2016). Despite the increasing number of spectroscopic and

molecular dynamic studies showing that  $(2\text{H})_{\text{Mg}}^{\times}$  is not a dominant defect in olivine, several studies continue to assert the opposite (e.g., Karato 2013, 2015; Dai & Karato 2014), even though such interpretations are not supported by their spectroscopic data. The occurrence of  $(2\text{H})_{\text{Mg}}^{\times}$  as a dominant OH-defect is often proposed because of the linear dependence of the hydrogen solubility with water fugacity. Indeed solubility law of hydrogen can be expressed by:

$$C_H = A f_{\text{H}_2\text{O}}^n \exp\left(-\frac{P\Delta V}{RT}\right) \quad (1)$$

where  $C_H$  is the concentration of hydrogen in the mineral,  $A$  a constant which essentially contains the entropy of reaction,  $f_{\text{H}_2\text{O}}$  the water fugacity,  $n$  an exponent related to the hydrogen incorporation mechanism, and  $\Delta V$  the volume change of the mineral due to the incorporation of hydrogen. An equation of this type is used to fit the experimental measurements, with the exponent  $n = 1$ . However the system is underdetermined. As shown by Férot and Bolfan-Casanova (2012) and Ingrin et al. (2013), several couples of  $(n, \Delta V)$  equally fit the data. We show here that natural high-pressure olivines contain the following OH-defects in various proportions, each with its correspondent exponent  $n$  and different  $\Delta V$ :  $(4\text{H})_{\text{Si}}^{\times}$  ( $n = 2$ ),  $(\text{OH})_{\text{i}}'$  ( $n = 0.5$ ),  $[(\text{Fe})_{\text{M}}^{\bullet}(\text{H})_{\text{M}}']^{\times}$  ( $n = 0.5$ ),  $(2\text{H})_{\text{Mg}}^{\times}$  ( $n = 1$ ). Therefore the actual solubility law related to the hydrogen incorporation mechanism would be a weighted sum of as many Eq. (1) as there are incorporation mechanisms. Given the number of unknowns, such a complex equation would obviously fit the experimental data but would be hardly manageable as long as the volume changes  $\Delta V$  are not accurately known for each incorporation mechanism. For simplicity, Eq. (1) can be used but the value of the exponent  $n$  cannot be taken as a robust indication of the

hydration mechanism.

From this detailed analysis of OH-defects, it is now possible to better interpret the results of previous experimental studies made from natural olivine rehydrated under pressure. For example, the study of hydrogen solubility in San Carlos olivine as a function of iron concentration (Zhao et al. 2004) actually shows the variation of OH-defects associated with  $\text{Ti}^{4+}$  and  $\text{Fe}^{3+}$  substitutions in the starting samples, more than a dependency in iron concentration. Their synthetic forsterite displays the typical bands associated with  $\text{Al}^{3+}$  (3350, 3344 and  $3322\text{ cm}^{-1}$ ) while the different annealed San Carlos olivine samples display the bands associated with  $\text{Fe}^{3+}$  ( $3356$  and  $3329\text{ cm}^{-1}$ ) in addition to the "titanoclinohumite" defect ( $3573$  and  $3525\text{ cm}^{-1}$ ). The analysis of these spectra in terms of defects associated with minor elements was not possible at the time of their publication because these hydrogen incorporation mechanisms into olivine were still unknown.

## 5. CONCLUSION

A comparison of low-temperature infrared spectra of pure forsterite and Fe-doped forsterite clearly shows the appearance of several bands in the high-frequency part of the spectrum, the most pronounced being located at  $3606$  and  $3599\text{ cm}^{-1}$  at  $-194^\circ\text{C}$ . The present theoretical study shows that the substitution of  $\text{Mg}^{2+}$  by  $\text{Fe}^{2+}$  in a neighboring octahedron of a hydrogarnet-type defect (i.e.  $[(4\text{H})_{\text{Si}}^x(\text{Fe})_{\text{M}}^x]^x$  defect) sufficiently alters the frequency of the OH bands to explain the additional bands observed. Similarly, in the low-frequency part of the OH vibrational spectrum, the presence of  $\text{Fe}^{2+}$  in the vicinity of

a doubly protonated Mg vacancy will increase the splitting of the vibrational modes and thus contribute to the broadening of the corresponding band.

With regard to  $\text{Fe}^{3+}$ , calculations show that OH-defects resulting from the substitution of a  $\text{Si}^{4+}$  by  $\text{Fe}^{3+}$  (i.e.  $(\text{Fe} + 1\text{H})_{\text{Si}}^{\times}$  defect) or the combination of a  $\text{Fe}^{3+}$  with a Si vacancy partially protonated (i.e.  $[(\text{Fe})_{\text{M}}^{\bullet}(3\text{H})'_{\text{Si}}]^{\times}$  defect) cannot explain any of the observed OH bands. Conversely, substitution of trivalent elements ( $\text{Fe}^{3+}$ ,  $\text{Al}^{3+}$ ,  $\text{Cr}^{3+}$ ) in octahedral site coupled to a M1 vacancy occupied by a  $\text{H}^{+}$  (i.e.  $[(\text{Fe,Al,Cr})_{\text{M}}^{\bullet}(1\text{H})'_{\text{M1}}]^{\times}$  defect) explains the presence of OH bands between 3310 and 3380  $\text{cm}^{-1}$ . The frequency and pleochroism of the theoretical bands are consistent with those observed in natural olivine samples (Berry et al. 2007; Tollan et al. 2015; this study). In particular, calculations confirm that the four bands commonly observed below 3400  $\text{cm}^{-1}$  in natural olivine (a couple at 3329 and 3355  $\text{cm}^{-1}$  and a couple at 3323 and 3358  $\text{cm}^{-1}$ ) are due to the substitution of  $\text{Mg}^{2+}$  by  $\text{Fe}^{3+}$  and  $\text{Cr}^{3+}$ , respectively ( $[(\text{Fe,Cr})_{\text{M}}^{\bullet}(1\text{H})'_{\text{M1}}]^{\times}$  defect).

The preponderance of these trivalent defects with the defect  $[(\text{Ti})_{\text{Mg}}^{\bullet\bullet}(2\text{H})'_{\text{Si}}]^{\times}$  in natural olivine, as well as the identification of OH-defects linked to boron and fluorine (e.g., Sykes et al. 1994; Ingrin et al. 2014; Crépeisson et al. 2014b), clearly evidence the prominent role of trace elements on hydrogen incorporation in lithospheric olivine. The important role of impurities on the properties of olivine was already stated more than twenty years ago by Wanamaker and Duba (1993) for electrical conductivity: “Even under controlled oxygen fugacities, olivine crystals from different localities and geological environments as well as specimens from the same locality often exhibit variations in electrical conductivity [Schock et al., 1989], presumably as a result of minor variations in trace element concentrations...” The present study confirms for water

speciation the acuity of this early statement. It demonstrates again the necessity to analyze and consider in a new light the results of solubility experiments made from natural olivine rehydrated under pressure and to integrate the individual contribution of OH-defects.

**Acknowledgements.** The authors thank the guest editor and an anonymous referee for their helpful comments. This work was performed using HPC resources from GENCI-IDRIS (Grant 2016-i2016041519) and was supported by CNRS through a grant from the INSU 2015-PNP program, and NSERC discovery grant to ACW. IK is grateful for the financial support of the Bolyai Postdoctoral Fellowship program.

## REFERENCES

- Aubaud, C., Bureau, H., Raepsaet, C., Khodja, H., Withers, A.C., Hirschmann, M.M., and Bell, D.R. (2009) Calibration of the infrared molar absorption coefficients for H in olivine, clinopyroxene and rhyolitic glass by elastic recoil detection analysis. *Chemical Geology*, 260, 286–294.
- Bai, Q., and Kohlstedt, D.L. (1992) Substantial hydrogen solubility in olivine and implications for water storage in the mantle. *Nature*, 357, 672-674.
- Bai, Q., and Kohlstedt, D.L. (1993) Effects of chemical environment on the solubility and incorporation mechanism for hydrogen in olivine. *Physics and Chemistry of Minerals*, 19, 460-471.
- Balan, E., Refson, K., Blanchard, M., Delattre, S., Lazzeri, M., Ingrin, J., Mauri, F., Wright, K., and Winkler, B. (2008) Theoretical infrared absorption coefficient of OH groups in minerals. *American Mineralogist*, 93, 950-953.
- Balan, E., Ingrin, J., Delattre, S., Kovacs, I., and Blanchard, M. (2011) Theoretical infrared spectrum of OH-defects in forsterite. *European Journal of Mineralogy*, 23, 285-292.
- Balan, E., Blanchard, M., Lazzeri M., and Ingrin, J. (2014) Contribution of interstitial OH groups to the incorporation of water in forsterite. *Physics and Chemistry of Minerals*, 41, 105-114.
- Bali, E., Bolfan-Casanova, N., and Koga, K.T. (2008) Pressure and temperature dependence of H solubility in forsterite: An implication to water activity in the Earth interior. *Earth and Planetary Science Letters*, 268, 354-363.



- Baroni, S., de Gironcoli, S., Dal Corso, A., and Giannozzi, P. (2001) Phonons and related crystal properties from density-functional perturbation theory. *Reviews of Modern Physics*, 73, 515-561.
- Bell, D.R., Rossman, G.R., Maldener, J., Endisch, D., and Rauch, F. (2003) Hydroxide in olivine: a quantitative determination of the absolute amount and calibration of the IR spectrum. *Journal of Geophysical Research*, 108, 2105–2113.
- Berry, A.J., Hermann, J., O'Neill, H.S.C., and Foran G.J. (2005) Fingerprinting the water site in mantle olivine. *Geology*, 33, 869-872.
- Berry, A.J., O'Neill, H.S.C., Hermann, J., and Scott D.R. (2007) The infrared signature of water associated with trivalent cations in olivine. *Earth and Planetary Science Letters*, 261, 134-142.
- Blanchard, M., Roberge, M., Balan, E., Fiquet, G., and Bureau, H. (2013) Infrared signatures of OH-defects in wadsleyite: A first-principles study. *American Mineralogist*, 98, 2132-2143.
- Braithwaite, J.S., Wright, K., and Catlow, C.R.A. (2003) A theoretical study of the energetics and IR frequencies of hydroxyl defects in forsterite. *Journal of Geophysical Research*, 108, 2284.
- Brodholt, J.P., and Refson, K. (2000) An ab initio study of hydrogen in forsterite and a possible mechanism for hydrolytic weakening. *Journal of Geophysical Research*, 105, 18977-18982.
- Brown, I.D. (2009) Recent developments in the methods and applications of the bond valence model. *Chemical Reviews*, 109, 6858-6919.

- Brown, I.D., and Altermatt, D. (1985) Bond-valence parameters obtained from a systematic analysis of the inorganic crystal structure database. *Acta Crystallographica*, B41, 244-247.
- Crépeisson, C., Bureau, H., Blanchard, M., Ingrin, J., and Balan, E. (2014a) Theoretical infrared spectrum of partially protonated cationic vacancies in forsterite. *European Journal of Mineralogy*, 26, 203-210.
- Crépeisson, C., Blanchard, M., Bureau, H., Sanloup, C., Withers, A.C., Khodja, H., Surblé, S., Béneut, K., Leroy, C., Giura, P., and Balan, E. (2014b) Clumped fluoride-hydroxyl defects in forsterite: Implications for the upper-mantle. *Earth and Planetary Science Letters*, 390, 287-295.
- Dai, L., and Karato, S. (2014) High and highly anisotropic electrical conductivity of the asthenosphere due to hydrogen diffusion in olivine. *Earth and Planetary Science Letters*, 408, 79-86.
- Demouchy, S., and Bolfan-Casanova, N. (2016) Distribution and transport of hydrogen in the lithospheric mantle: A review. *Lithos*, 240-243, 402-425.
- Donnay, G., and Allmann, R. (1970) How to recognize  $O^{2-}$ ,  $OH^-$ , and  $H_2O$  in crystal structures determined by X-rays. *American Mineralogist*, 55, 1003-1015.
- Férot, A., and Bolfan-Casanova, N. (2012) Water storage capacity in olivine and pyroxene to 14 GPa: Implications for the water content of the Earth's upper mantle and nature of seismic discontinuities. *Earth and Planetary Science Letters*, 349, 218-230.
- Fujino, K., Sasaki, S., Takeuchi, Y., and Sadanaga, R. (1981) X-ray determination of electron distributions in forsterite, fayalite and tephroite. *Acta Crystallographica*

Section B, 37, 513-518.

- Gaetani, G.A., O'Leary J.A., Koga, K.T., Hauri E.H., Rose-Koga E.F., and Monteleone, B.D. (2014) Hydration of mantle olivine under variable water and oxygen fugacity conditions. *Contributions to Mineralogy and Petrology*, 167, 965-979.
- Giannozzi, P., Baroni, S., Bonini, N., Calandra, M., Car, R., Cavazzoni, C., Ceresoli, D., Chiarotti, G.L., Cococcioni, M., Dabo, I., Dal Corso, A., de Gironcoli, S., Fabris, S., Fratesi, G., Gebauer, R., Gerstmann, U., Gougoussis, C., Kokalj, A., Lazzeri, M., Martin-Samos, L., Marzari, N., Mauri, F., Mazzarello, R., Paolini, S., Pasquarello, A., Paulatto, L., Sbraccia, C., Scandolo, S., Sclauzero, G., Seitsonen, A.P., Smogunov, A., Umari, P., and Wentzcovitch, R.M. (2009) Quantum ESPRESSO: a modular and open-source software project for quantum simulations of materials. *Journal of Physics: Condensed Matter*, 21, 395502.
- Grant, K.J., Brooker, R.A., Kohn, S.C., and Wood, B.J. (2007a) The effect of oxygen fugacity on hydroxyl concentrations and speciation in olivine: Implications for water solubility in the upper mantle. *Earth and Planetary Science Letters*, 261, 217-229.
- Grant, K., Ingrin, J., Lorand J-P., and Dumas, P. (2007b) Water partitioning between mantle minerals from peridotite xenoliths. *Contribution to Mineralogy and Petrology*, 154, 15-34.
- Haiber, M., Ballone, P., and Parrinello, M. (1997) Structure and dynamics of protonated  $\text{Mg}_2\text{SiO}_4$ : An ab-initio molecular dynamics study. *American Mineralogist*, 82, 913-922.

- Ingrin, J., Liu, J., Depecker, C., Kohn, S.C., Balan, E., and Grant, K.J. (2013) Low-temperature evolution of OH bands in synthetic forsterite, implication for the nature of H-defects at high pressure. *Physics and Chemistry of Minerals*, 40, 499-510.
- Ingrin, J., Kovács, I., Deloule, E., Balan, E., Blanchard, M., Kohn, S.C., and Hermann, J. (2014) Identification of hydrogen defects linked to boron substitution in synthetic forsterite and natural olivine. *American Mineralogist*, 99, 2138-2141.
- Karato, S. (2013) Theory of isotope diffusion in a material with multiple species and its implications for hydrogen-enhanced electrical conductivity in olivine. *Physics of the Earth and Planetary interiors*, 219, 49-54.
- Karato, S. (2015) Some notes on hydrogen-related point defects and their role in the isotopic exchange and electrical conductivity in olivine. *Physics of the Earth and Planetary interiors*, 248, 94-98.
- Kohlstedt, D.J., Keppler, H., and Rubie, D.C. (1996) Solubility of water in the *a*, *b*, and *g* phases of  $(\text{Mg,Fe})_2\text{SiO}_4$ . *Contributions to Mineralogy and Petrology*, 123, 345-357.
- Kovács, I., O'Neill, H.St.C., Hermann, J., and Hauri, E.H. (2010) Sitespecific infrared OH absorption coefficients for water substitution into olivine. *American Mineralogist*, 95, 292–299.
- Kovács, I., Green, D.H., Rosenthal, A., Hermann, J., O'Neil H.St.C., Hibberson W.O., and Udvardi B. (2012) An experimental study of water in Nominally Anhydrous Minerals in the upper mantle near the water-saturated solidus. *Journal of Petrology*, 53, 2067-2093.

- Kröger, F.A., and Vink, H.J. (1956) Relation between the concentrations of imperfections in crystalline solids. *Solid State Physics*, 3, 307-435.
- Lemaire, C., Kohn, S.C., and Brooker, R.A. (2004) The effect of silica activity on the incorporation mechanism of water in synthetic forsterite: a polarised infrared spectroscopic study. *Contributions to Mineralogy and Petrology*, 147, 48-57.
- Litasov, K.D., Ohtani, E., Kagi, H., and Jacobsen, S.D. (2007) Temperature dependence and mechanism of hydrogen incorporation in olivine at 12.5-14.0 GPa. *Geophysical Research Letters*, 34, L16314.
- Litasov, K.D., Shatskiy, A.F., Pal'yanov, Y.N., Sokol, A.G., Katsura, T., and Ohtani, E. (2009) Hydrogen incorporation into forsterite in  $\text{Mg}_2\text{SiO}_4\text{-K}_2\text{Mg}(\text{CO}_3)_2\text{-H}_2\text{O}$  and  $\text{Mg}_2\text{SiO}_4\text{-H}_2\text{O-C}$  at 7.5–14.0 GPa. *Russian Geology and Geophysics*, 50, 1129-1138.
- McCammom, C.A., Frost, D.J., Smyth, J.R., Laustsen, H.M.S., Kawamoto, T., Ross, N.L., and van Aken, P.A. (2004) Oxidation state of iron in hydrous mantle phases: Implications for subduction and mantle oxygen fugacity. *Physics of the Earth and Planetary interiors*. 143-144, 157-169.
- McCarty, R.J., Palke, A.C., Stebbins, J.F., and Hartman J.S. (2015) Transition metal cation site preferences in forsterite ( $\text{Mg}_2\text{SiO}_4$ ) determined from paramagnetically shifted NMR resonances. *American Mineralogist*, 100, 1265-1276.
- Mosenfelder, J.L., Deligne, N.I., Asimow, P.D., and Rossman, G.R. (2006) Hydrogen incorporation in olivine from 2-12 GPa. *American Mineralogist*, 91, 285-294.

- Otsuka, K., and Karato, S. (2011) Control of the water fugacity at high pressures and temperatures: Applications to the incorporation mechanisms of water in olivine. *Physics of the Earth and Planetary Interiors*, 189, 27-33.
- Perdew, J.P., Burke, K., and Ernzerhof, M. (1996) Generalized Gradient Approximation Made Simple. *Physical Review Letters*, 77, 3865–3868.
- Rossman, G.R. (2006) Analytical methods for measuring water in nominally anhydrous minerals. *Water in Nominally Anhydrous Minerals*. American Mineralogical Society Geochemical Society, Chantilly (Vir.), pp. 1–28.
- Schmädicke, E., Gose, J., Witt-Eickschen, G., and Brätz, H. (2013) Olivine from spinel peridotite xenoliths: Hydroxyl incorporation and mineral composition. *American Mineralogist*, 98, 1870-1880.
- Schock, R.N., Dubal, A.G., and Shankland, T.J. (1989) Electrical conduction in olivine. *Journal of Geophysical Research*, 94, 5829-5839.
- Shaw, D.M., and Tse, J.S. (2007) Vibrational dynamics of H<sup>+</sup>-substituted forsterite: A first-principles molecular dynamics study. *American Mineralogist*, 92, 1593-1600.
- Smyth, J.R., Frost, D.J., Nestola, F., Holl, C.M., and Bromiley, G. (2006) Olivine hydration in the deep upper mantle: Effects of temperature and silica activity. *Geophysical Research Letters*, 33, L15301.
- Sykes, D., Rossman, G.R., Veblen, D.R., and Grew, E.S. (1994) Enhanced H and F incorporation in borian olivine. *American Mineralogist*, 79, 904-908.
- Tollan, P.M.E., O'Neill, H.St.C., Hermann, J., Benedictus, A., and Arculus, R.J. (2015) Frozen melt-rock reaction in a peridotite xenolith from sub-arc mantle recorded

by diffusion of trace elements and water in olivine. *Earth and Planetary Science Letters*, 422, 169-181.

Umemoto, K., Wentzcovitch, R.M., Hirschmann, M.M., Kohlstedt, D.L., and Withers, A.C. (2011) A first-principles investigation of hydrous defects and IR frequencies in forsterite: The case for Si vacancies. *American Mineralogist*, 96, 1475-1479.

Walker, A.M., Demouchy, S., and Wright, K. (2006) Computer modelling of the energetics and vibrational properties of hydroxyl groups in  $\alpha$ - and  $\beta$ -Mg<sub>2</sub>SiO<sub>4</sub>. *European Journal of Mineralogy*, 18, 529-543.

Walker, A.M., Hermann, J., Berry, A.J., and O'Neill, H.St.C. (2007) Three water sites in upper mantle olivine and the role of titanium in the water weakening mechanism. *Journal of Geophysical Research*, 112, B05211.

Wanamaker, B.J., and Duba, A.G. (1993) Electrical conductivity of San Carlos olivine along [100] under oxygen- pyroxene-buffered conditions and implications for defect equilibria. *Journal of Geophysical Research*, 98, 489-500.

Withers, A.C., and Hirschmann, M.M. (2008) Influence of temperature, composition, silica activity and oxygen fugacity on the H<sub>2</sub>O storage capacity of olivine at 8 GPa. *Contributions to Mineralogy and Petrology*, 156, 595-605.

Withers, A.C., Hirschmann, M.M., and Tenner, T.J. (2011) The effect of Fe on olivine H<sub>2</sub>O storage capacity: Consequences for H<sub>2</sub>O in the Martian mantle. *American Mineralogist*, 96, 1039-1053.

Withers, A.C., Bureau, H., Raepsaet, C., and Hirschmann, M.M. (2012) Calibration of infrared spectroscopy by elastic recoil detection analysis of H in synthetic olivine. *Chemical Geology*, 334, 92-98.

- Xue, X., Kanzaki, M., Turner, D., and Loroche, D. (2016) Hydrogen incorporation mechanisms in forsterite:  $^1\text{H}$  NMR measurement and first-principles calculation. Goldschmidt Conference Abstract, 3503.
- Yang, X. (2016) Effect of oxygen fugacity on OH dissolution in olivine under peridotite-saturated conditions: An experimental study at 1.5-7 GPa and 1100-1300°C. *Geochimica et Cosmochimica Acta*, 173, 319-336.
- Zhao, Y.H., Ginsberg, S.B., and Kohlstedt, D.J. (2004) Solubility of hydrogen in olivine: dependence on temperature and iron content. *Contributions to Mineralogy and Petrology*, 147, 155-161.



## FIGURE CAPTIONS

**FIGURE 1.** Unpolarized low-temperature infrared spectrum of a H-doped forsterite (Fo100 synthesized at 2 GPa, 1400-1275°C, green line, Lemaire et al. 2004; Ingrin et al. 2014) compared with polarized spectra of a H-doped olivine Fo<sub>91</sub> synthesized at 6 GPa, 1250°C (Withers et al. 2011). Red lines are for polarization // to Y and black lines for polarization perpendicular to Y with X and Z components. The new absorption bands compared with Mg end-member forsterite are at 3606, 3599, 3560, 3551 and 3543 cm<sup>-1</sup>. The vertical line is a guide for the eyes. Spectra of Fo<sub>91</sub> were acquired with a 2 cm<sup>-1</sup> resolution.

**FIGURE 2.** Polarized infrared spectra of single crystals [2] (X,Z) and [6] (X,Y) of the KHL8306 olivine (Fo<sub>91</sub>) at 25°C and -194°C. Spectra were acquired at 4 cm<sup>-1</sup> and 1 cm<sup>-1</sup> resolution at 25°C and -194°C, respectively.

**FIGURE 3.** Theoretical polarized infrared spectra of [(4H)<sub>Si</sub><sup>x</sup>(Fe)<sub>M</sub><sup>x</sup>]<sup>x</sup> defects (left) where the Fe<sup>2+</sup> sits either in the M1 or M2 site sharing a corner with the Si vacancy. The theoretical infrared spectrum of (4H)<sub>Si</sub><sup>x</sup> in pure forsterite is given for comparison (= Si<sub>3</sub> configuration in Balan et al. 2011). Structural model (right) with Mg in yellow, Fe in brown, Si in blue, O in red and H in white (color online).

**FIGURE 4.** Theoretical polarized infrared spectra of [(2H)<sub>M1</sub><sup>x</sup>(Fe)<sub>M</sub><sup>x</sup>]<sup>x</sup> defects (left) and structural models (right). Fe<sup>2+</sup> sits either in the M1 site sharing an edge with the

protonated M1 vacancy or in the M2 site sharing a corner with the M1 vacancy. The theoretical IR spectrum of  $(2\text{H})_{\text{M1}}^{\times}$  in pure forsterite is given for comparison (Balan et al. 2011).

**FIGURE 5.** Theoretical polarized infrared spectra of  $[(\text{Fe},\text{Al},\text{Cr})_{\text{M}}^{\bullet}(\text{1H})'_{\text{M1}}]^{\times}$  defects. The bold black line, the thin black line and the thin grey line represent the relative stability of the defects (Table 2). Vertical dashed lines mark the position of the two most intense bands observed in natural olivine from Kilbourne Hole (this study, Fig. 2). Corresponding structural models are displayed in Fig. 6.

**FIGURE 6.** Structural models of  $[(\text{Fe},\text{Al},\text{Cr})_{\text{M}}^{\bullet}(\text{1H})'_{\text{M1}}]^{\times}$  defects.

**FIGURE 7.** Theoretical integrated molar absorption coefficients of OH stretching modes as a function of their average vibrational frequency. Previous data (crosses and open symbols) are from Balan et al. (2011; 2014), Crépisson et al. (2014a; 2014b), Ingrin et al. (2014). The solid line corresponds to the general theoretical correlation determined by Balan et al. (2008). The dashed line is a guide for the eye.

## TABLES

**Table 1.** Wavenumbers (in  $\text{cm}^{-1}$ ) and polarization of OH stretching bands (direction of the electric field) in the olivine investigated here (Figs. 1 and 2)

Sample	Wavenumber at $-194^\circ\text{C}$	Wavenumber at $25\text{-}27^\circ\text{C}$	Shift	Polarization	Proposed assignment
Synthetic olivine Fo100 * Lemaire et al. 2004; Ingrin et al. 2013, 2014 2 GPa, $1400\text{-}1275^\circ\text{C}$	3566	3550	-16	Y	$(\text{OH})'_i$
	3568	3566	-2	Z	$(4\text{H})_{\text{Si}}^x$
	3582	3579	-3	X > Y	$(4\text{H})_{\text{Si}}^x$
	3615	3613	-2	X	$(4\text{H})_{\text{Si}}^x$
Synthetic olivine Fo91 M449 Withers et al. 2011 6 GPa, $1250^\circ\text{C}$	3528	?	?	X, Z>Y	$[(4\text{H})_{\text{Si}}^x(\text{Fe})_{\text{M2}}^x]^x$
	3543	3538?	-5	X, Z>Y	$[(4\text{H})_{\text{Si}}^x(\text{Fe})_{\text{M2}}^x]^x$
	3551	3549?	-2	X,Y,Z	$[(4\text{H})_{\text{Si}}^x(\text{Fe})_{\text{M1}}^x]^x$
	3560	?		Y	$[(4\text{H})_{\text{Si}}^x(\text{Fe})_{\text{M1}}^x]^x$
	3567	3550	-17	Y	$(\text{OH})'_i$
	3568	3566	-2	Z	$(4\text{H})_{\text{Si}}^x$
	3582	3579	-3	X > Y	$(4\text{H})_{\text{Si}}^x$
	3599	3598?	-1	X>>Z**	$[(4\text{H})_{\text{Si}}^x(\text{Fe})_{\text{M2}}^x]^x$
	3606	3600?	-6	X>>Z**	$[(4\text{H})_{\text{Si}}^x(\text{Fe})_{\text{M1}}^x]^x$
	3615	3613	-2	X	$(4\text{H})_{\text{Si}}^x$
Natural olivine Fo91 KHL8306	3313	3310	-3	Z >> X	n.d.
	3332	3329	-3	Z >> X	$[(\text{Fe})_{\text{M1}}^x(\text{1H})'_{\text{M1}}]^x$

1.74 GPa, 1034°C	3390	3384	-6	Z > X	n.d.
	3529	3525	-4	X	$[(\text{Ti})_{\text{M1}}^{\bullet\bullet}(\text{2H})_{\text{Si}}^{\prime\prime}]^{\times}$
	3576	3573	-3	X	$[(\text{Ti})_{\text{M1}}^{\bullet\bullet}(\text{2H})_{\text{Si}}^{\prime\prime}]^{\times}$

\* Polarization data from Lemaire et al. (2004). \*\* Polarization data from Withers et al. (2011)

? These bands are too broad and convoluted to be separated from others at room temperature.

X, Y, Z correspond to the crystallographic directions [100], [010] and [001], respectively.

**Table 2.** Theoretical properties of the investigated OH-defects

Defect	Relative energy (meV)	d(O-H) (Å)	OH-stretching wavenumber (cm <sup>-1</sup> )	K <sub>int</sub> (L mol <sup>-1</sup> cm <sup>-2</sup> )	Contribution to total absorbance (%)
$[(4\text{H})_{\text{Si}}^{\times}(\text{Fe})_{\text{M1corner}}^{\times}]^{\times}$	0	O1-H 0.983	3572*	50420	40
		O2-H 0.985	3555*		26
		O3-H 0.984	3530*		16
		O3-H 0.984	3518*		18
$[(4\text{H})_{\text{Si}}^{\times}(\text{Fe})_{\text{M2corner}}^{\times}]^{\times}$	43	O1-H 0.983	3574*	45180	7
		O2-H 0.984	3559*		62
		O3-H 0.984	3519*		14
		O3-H 0.984	3510*		17
$[(2\text{H})_{\text{M1}}^{\times}(\text{Fe})_{\text{M1}}^{\times}]^{\times}$	0	O2-H 1.002	3237	185060	60
		O2-H 1.005	3184		40
$[(2\text{H})_{\text{M1}}^{\times}(\text{Fe})_{\text{M2}}^{\times}]^{\times}$	3	O2-H 1.001	3252	158570	63
		O2-H 1.004	3213		37
$(2\text{H})_{\text{M2}}^{\times}\text{A}$	0	O3-H 1.002	3265*	198010	78
		O3-H 1.002	3247*		22

$(2\text{H})_{\text{M2}}^{\times} \text{B}$	58	O3-H 0.989	3488	148460	32
		O3-H 1.005	3209		68
$[(\text{Fe})_{\text{M2edge}}^{\bullet} (\text{1H})'_{\text{M1}}]^{\times}$	0	O3-H 0.996	3388	98115	-
$[(\text{Fe})_{\text{M2corner}}^{\bullet} (\text{1H})'_{\text{M1}}]^{\times}$	32	O2-H 1.003	3246	142000	-
$[(\text{Fe})_{\text{M1edge}}^{\bullet} (\text{1H})'_{\text{M1}}]^{\times}$	39	O2-H 0.996	3374	121770	-
$[(\text{Al})_{\text{M2edge}}^{\bullet} (\text{1H})'_{\text{M1}}]^{\times}$	0	O3-H 0.996	3384	100800	-
$[(\text{Al})_{\text{M1edge}}^{\bullet} (\text{1H})'_{\text{M1}}]^{\times} \text{A}$	12	O2-H 0.996	3385	104620	-
$[(\text{Al})_{\text{M1edge}}^{\bullet} (\text{1H})'_{\text{M1}}]^{\times} \text{B}$	30	O3-H 0.995	3401	95000	-
$[(\text{Cr})_{\text{M1edge}}^{\bullet} (\text{1H})'_{\text{M1}}]^{\times} \text{A}$	0	O2-H 0.997	3366	120720	-
$[(\text{Cr})_{\text{M1edge}}^{\bullet} (\text{1H})'_{\text{M1}}]^{\times} \text{B}$	22	O3-H 0.995	3406	89430	-
$(\text{Fe} + \text{1H})_{\text{Si}}^{\times}$	-	O3-H 1.003	3140	309500	-
$[(\text{Fe})_{\text{M1}}^{\bullet} (\text{3H})'_{\text{Si}}]^{\times}$	-	O3-H 0.984	3544	90580	30
		O3-H 0.988	3474		24
		O1-H 0.997	3255		46

\*modes involving a coupled motion of two or more OH groups.

A and B allow to distinguish two defect configurations having the same Kröger-Vink notation.

FIGURE 1.

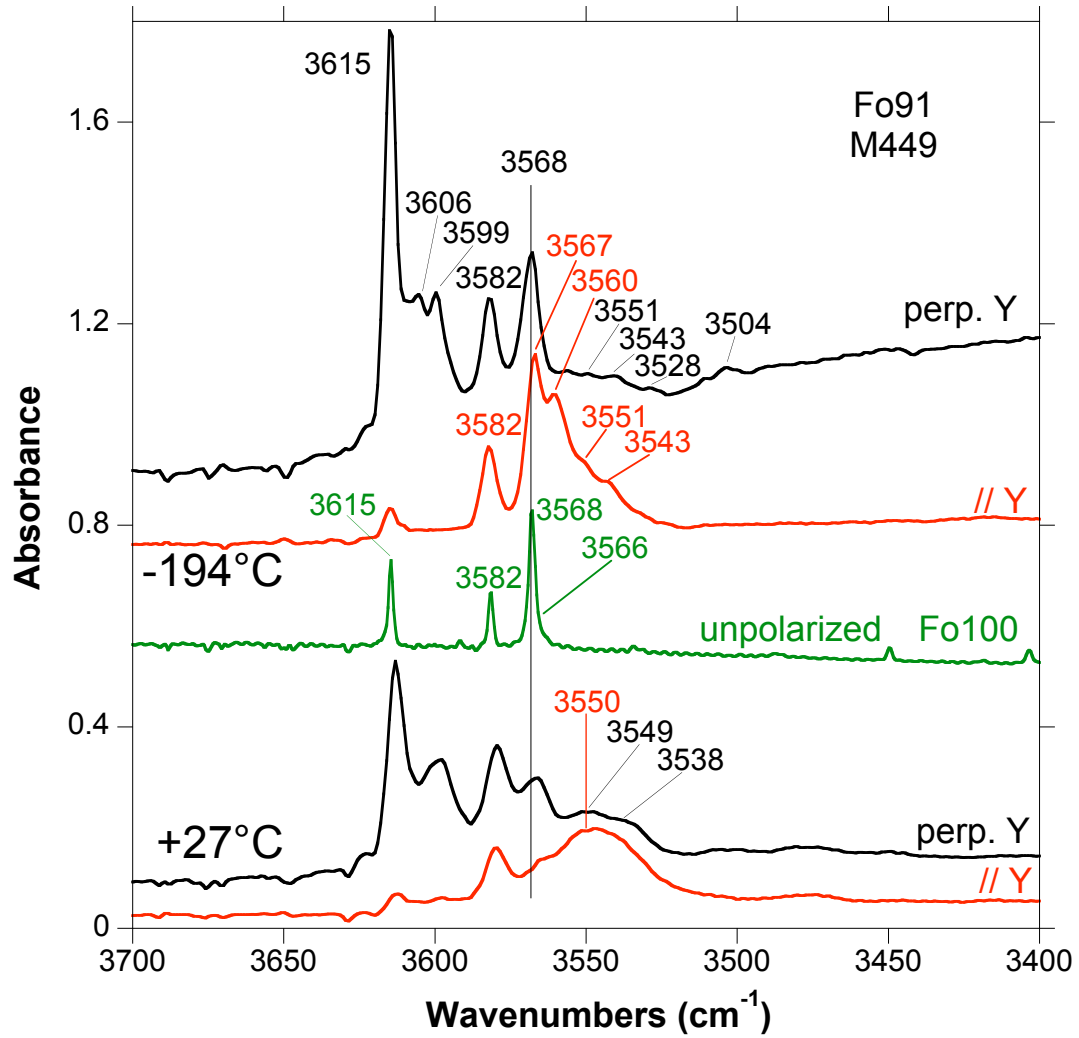


FIGURE 2.

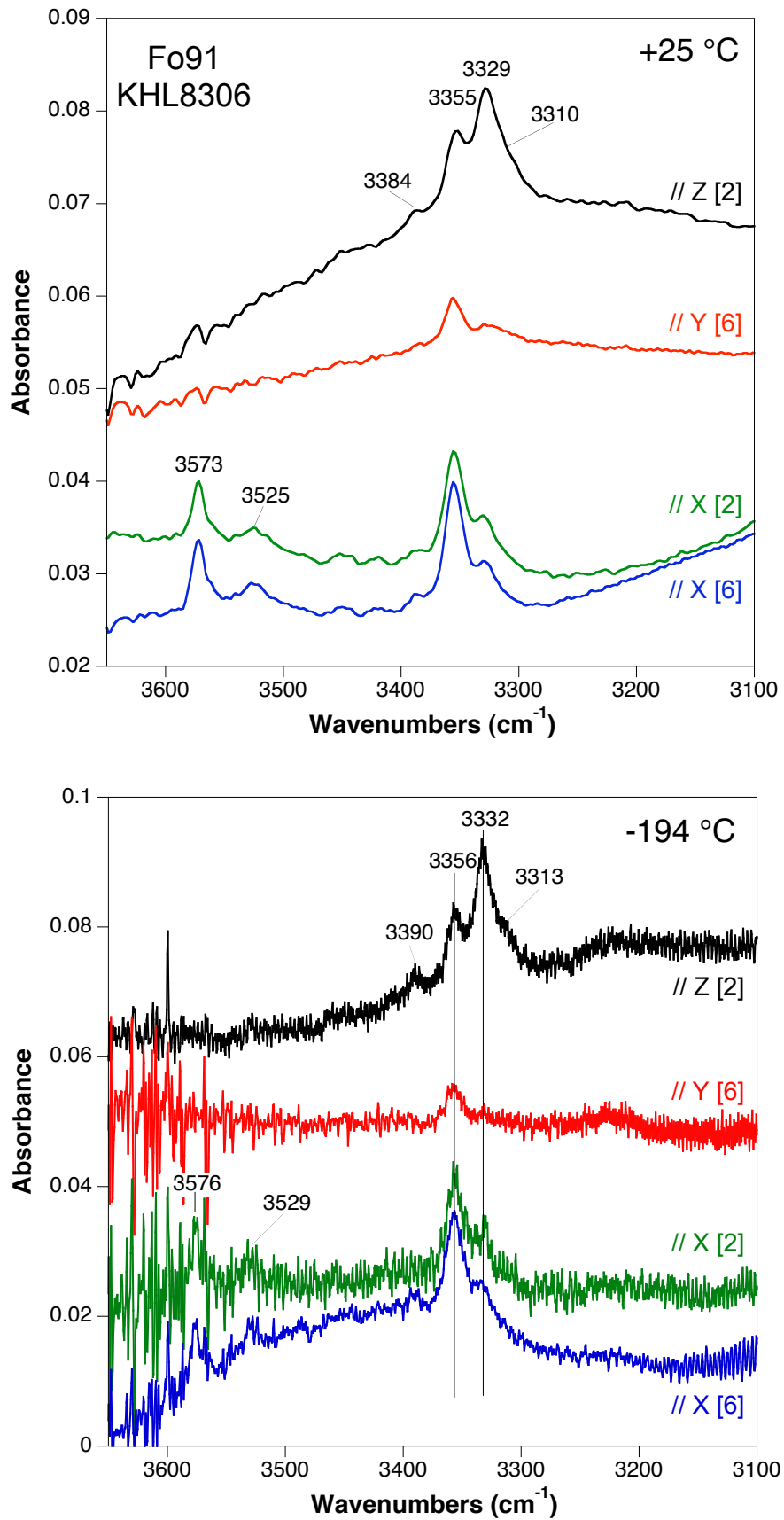


FIGURE 3.

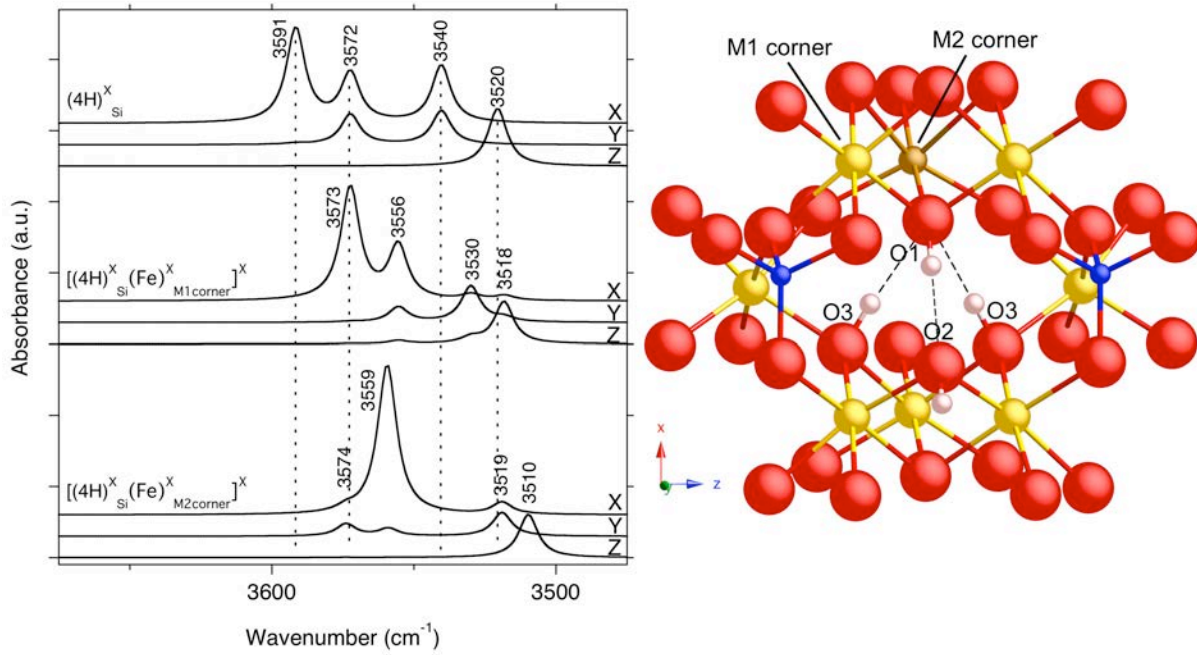




FIGURE 4.

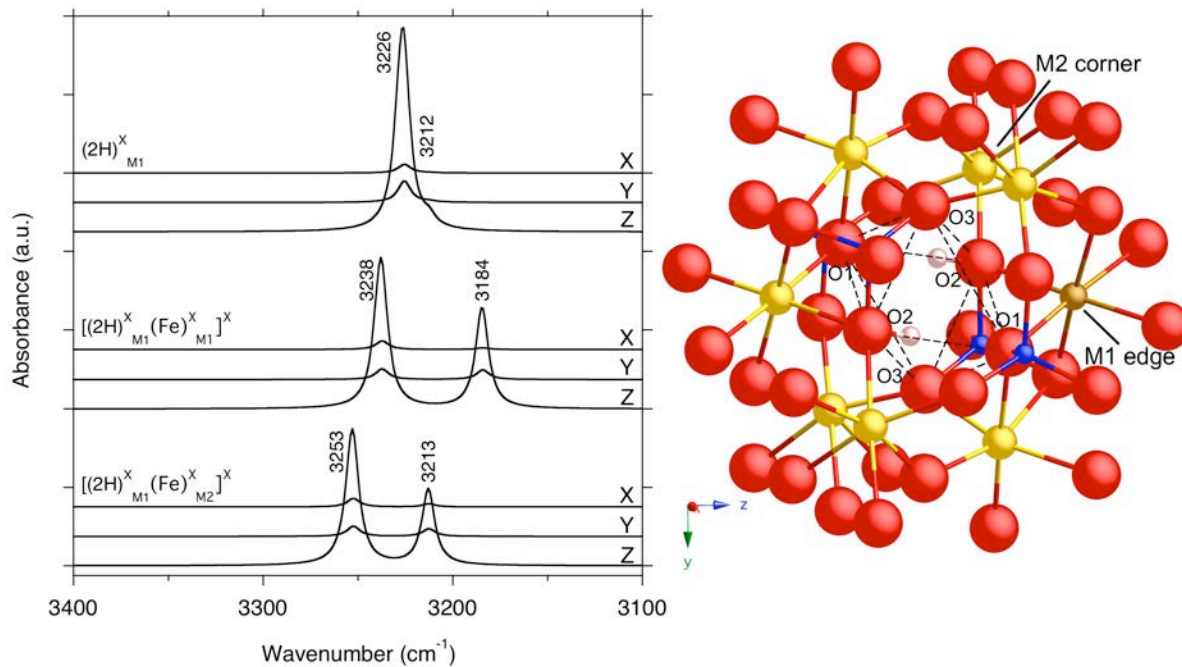


FIGURE 5.

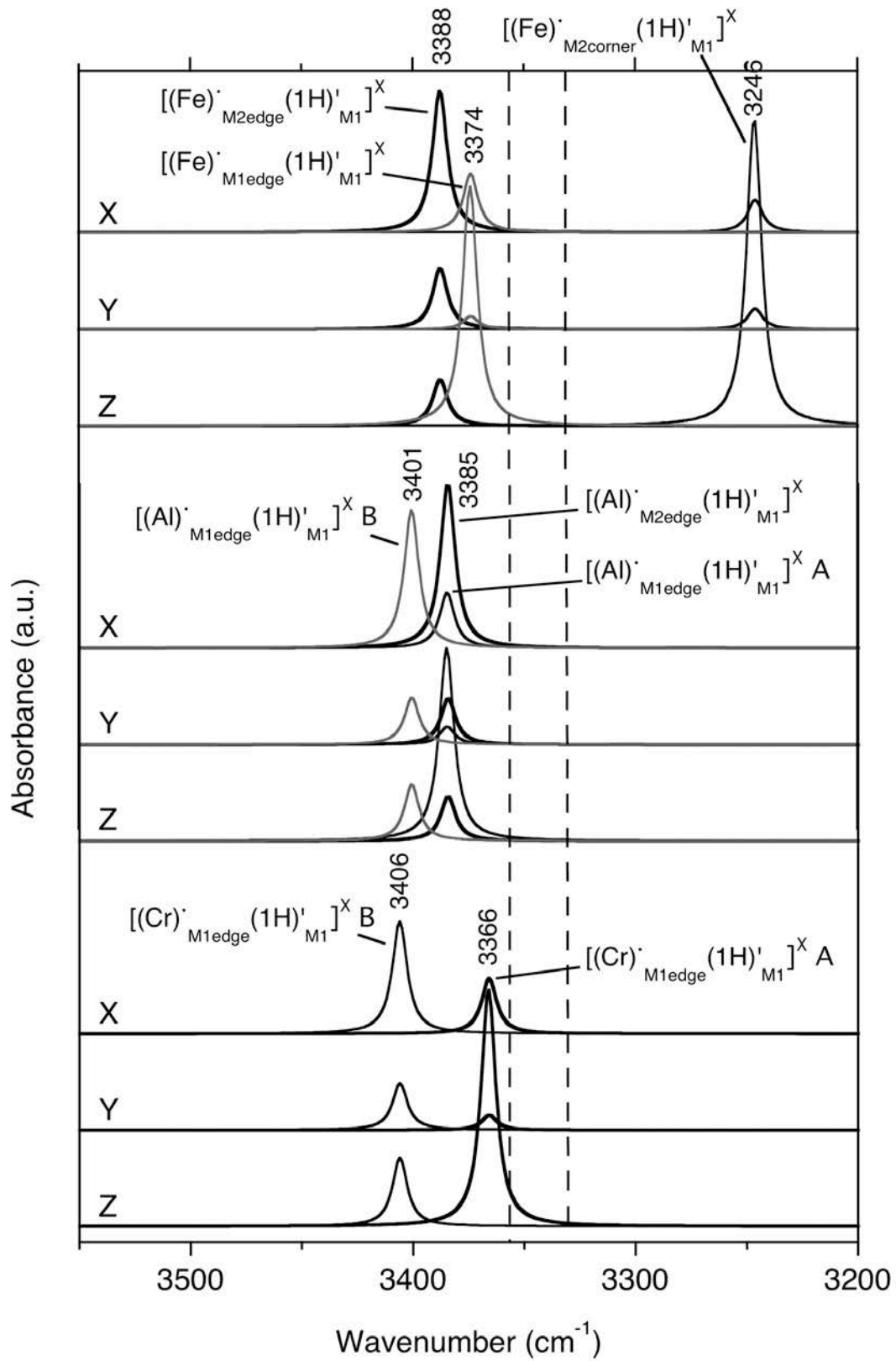


FIGURE 6.

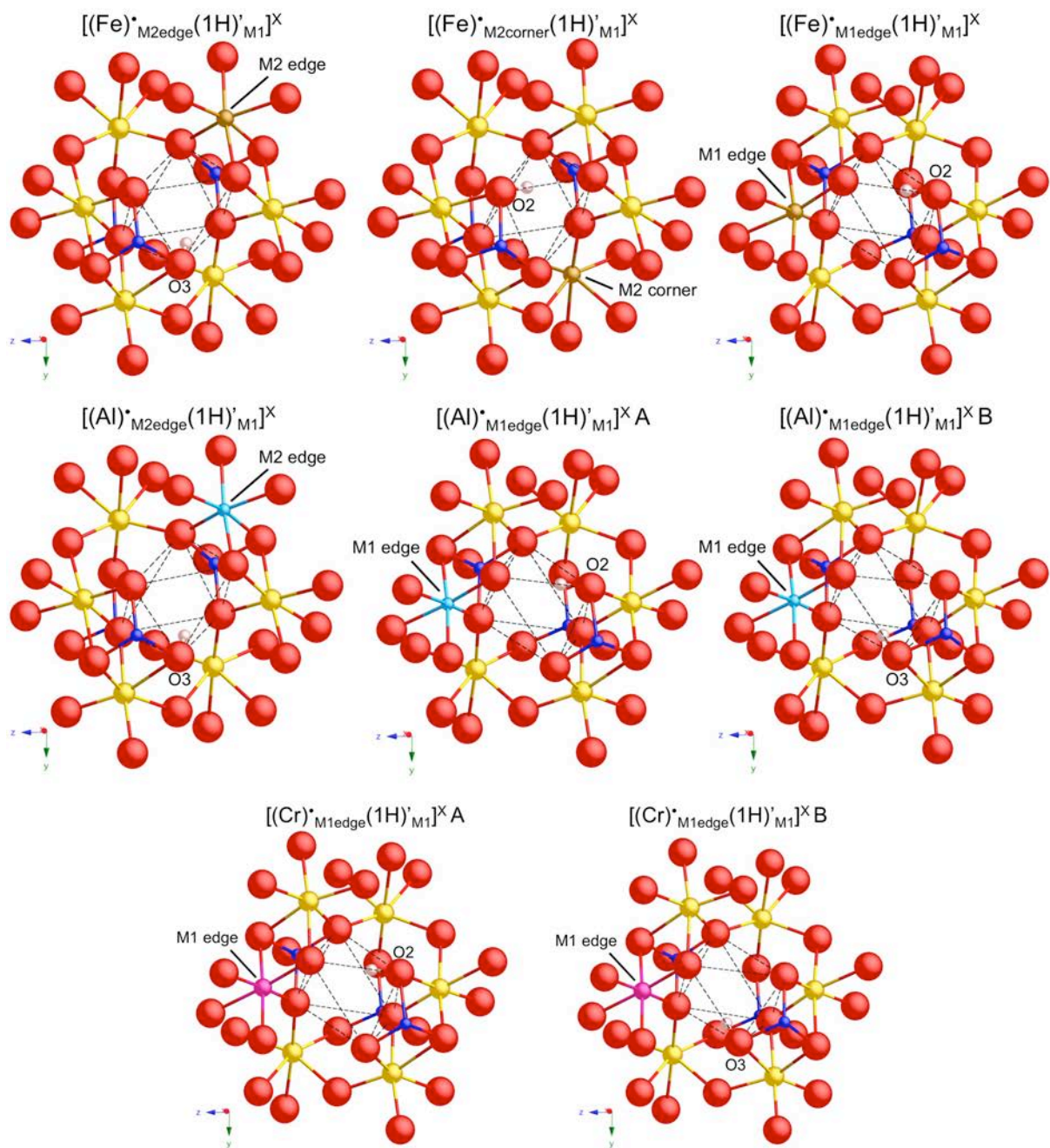


FIGURE 7.

